

Journal of

[www. biophotonics-journal.org](http://www.biophotonics-journal.org)

BIOPHOTONICS

 **WILEY-VCH**

REPRINT

FULL ARTICLE

Photothermal bleaching in time-lapse photoacoustic microscopy

Liang Gao**, Lidai Wang**, Chiye Li, Alejandro Garcia-Uribe, and Lihong V. Wang*

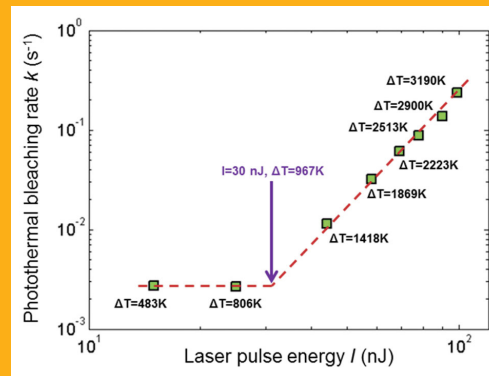
Department of Biomedical Engineering, Washington University in St. Louis, One Brookings Dr., St. Louis, MO, 63130, USA

Received 11 September 2012, revised 23 October 2012, accepted 25 October 2012

Published online 26 November 2012

Key words: photoacoustic microscopy, nanoparticle, photothermal bleaching, timelapse imaging

We studied the phenomenon of photothermal bleaching – a gradual reduction of contrast agent particles during repeated scans in photoacoustic microscopy. The dependence of the photothermal bleaching rate on the excitation pulse energy, pulse duration, and the absorber's size was determined while the laser focal diameter was held constant. Our results showed that the dependence of the photothermal bleaching rate on the excitation pulse energy differed before and after the absorbers were raised to their melting point by the deposited laser energy. Based on this finding, we suggested an optimal excitation pulse energy, which balances the photothermal bleaching rate and signal amplitude, for time-lapse imaging applications.



Dependence of photothermal bleaching rate k on the delivered laser pulse energy and temperature rise.

1. Introduction

Photobleaching, a common phenomenon in fluorescence microscopy, occurs when a fluorophore permanently loses its ability to fluoresce due to long exposure to intense excitation light [1, 2]. On the one hand, photobleaching undesirably limits the observation time for monitoring a dynamic process; on the other hand, photobleaching can be beneficially employed in molecular diffusion or motion studies via techniques such as fluorescence-recovery after photobleaching (FRAP) [3, 4] or fluorescence loss in photobleaching (FLIP) [5]. Properly exploiting photobleaching requires a thorough understanding

of its dependence on the excitation light power. Such a dependence in fluorescence microscopy has been carefully characterized [1, 2, 6].

However, photobleaching is not exclusively a feature of fluorescence microscopy: It also exists in other imaging modalities. One example is photoacoustic microscopy (PAM) [7, 8], in which the sample is irradiated by a short laser pulse (ns duration). The absorbed light energy is converted into heat and produces an ultrasonic wave via thermoelastic expansion. The ultrasonic wave is detected by an ultrasound transducer. Contrasts in PAM stem from light absorption by endogenous or exogenous absorbers, such as hemoglobin [9] or nanoparticles [10, 11], re-

* Corresponding author: e-mail: lhwang@wustl.edu

** Authors contributed equally to this work.

spectively. These absorbers can be intentionally photo-destroyed using strong excitation light, resulting in a gradual reduction of photoacoustic signals during repeated scans.

The photobleaching mechanism in PAM differs from that in fluorescence microscopy. Upon absorbing a photon, an electron transits from the ground state to an excited state. The electron's energy can be released via primarily two paths: radiative decay, i.e., fluorescence, or non-radiative decay, i.e., thermal dissipation. In fluorescence microscopy, photobleaching is the photochemical destruction of a fluorophore – during radiative decay the excited electrons are trapped in a relatively long-lived triplet state (lifetime $\sim 1 \mu\text{s}$), thus allowing the fluorophore a much longer time to undergo irreversible chemical reactions with the environment than would be allowed by the singlet-singlet transition [12]. In PAM, photobleaching is the photothermal destruction of an absorber – the heat generated during non-radiative decay alters the structure of the absorber, thus reducing sample's absorption coefficient at the original excitation wavelength. As an example, Figure 1 shows the scanning electron microscopic images of 100 nm gold nanoparticles (GNPs) before and after they were imaged by PAM. The GNPs were fragmented by the deposited laser energy during photoacoustic imaging and thus vanished. To distinguish the photobleaching in PAM from its fluorescent counterpart, we term this photothermally induced absorption change as “photothermal bleaching”.

To begin to exploit the photothermal bleaching in PAM, here we studied its dependence on the laser pulse energy, the absorber's diameter, and the laser pulse duration while the laser focal diameter was held constant. GNPs were chosen as the targets because they were widely used as contrast agents in photoacoustic imaging applications [10, 11, 13]. Our results revealed that, within the linear excitation range, photothermal bleaching behaved differently before and after the GNPs were raised to their melt-

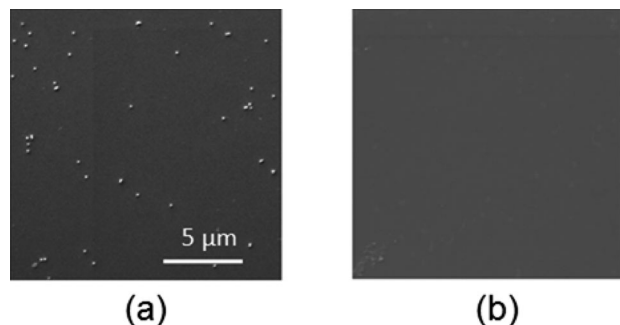


Figure 1 Photothermal destruction of contrast agents in PAM. Scanning electron microscopic images of a sample with 100 nm GNPs fixed on a cover glass (a) before and (b) after it was imaged by PAM at an intentionally high fluence of 82.6 mJ/cm^2 .

ing point. Below this critical point, the photothermal bleaching rate had weak dependence on the laser pulse energy; while above the melting point, the photothermal bleaching rate increased rapidly. Based on this finding, we suggest a method to determine the optimal excitation laser pulse energy for time-lapse photoacoustic imaging.

2. Results and discussion

To confine our studies within the linear photoacoustic imaging range, where the photoacoustic signal amplitude is proportional to the laser pulse energy, we first identified the pulse energy range for linear excitation. GNPs of 400 nm in diameter were suspended in water solution and imaged by a PAM system [14] using different pulse energies. Since GNPs diffuse freely in the water solution, the photothermally bleached particles were rapidly replaced, and thus negligible. The measured photoacoustic amplitude versus laser pulse energy is shown in Figure 2. Below $\sim 120 \text{ nJ}$ (fluence: 0.33 J/cm^2), photoacoustic amplitude is linearly related to the pulse energy, so laser pulse energies within this linear range were used in the following experiments. The focal diameter of the laser beam was set to $6.8 \mu\text{m}$ for all experiments, and the laser wavelength was 532 nm.

Next, the 400 nm-diameter GNPs were fixed on a cover glass to eliminate the effect of diffusion on the measurement of photothermal bleaching rate (see Materials and methods). The photothermal bleaching dynamics were measured under different laser pulse energies, and the results are shown in Figure 3. The photothermal bleaching rate k was calculated by fitting a double exponential curve to the acquired data (see Materials and methods).

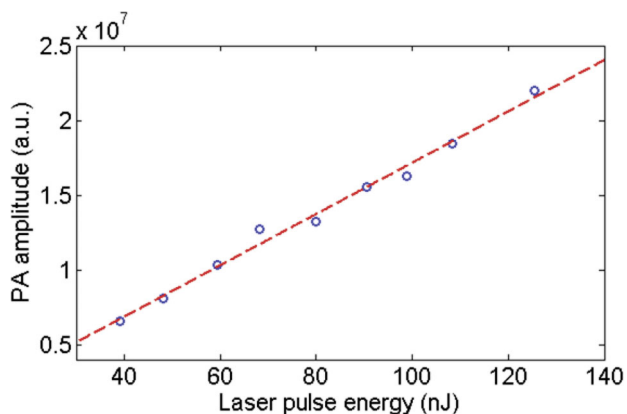


Figure 2 Photoacoustic amplitude vs. delivered excitation laser pulse energy. The 400-nm-diameter GNPs were suspended in water solution and imaged by PAM. The coefficient of determination, R^2 , was 0.990.

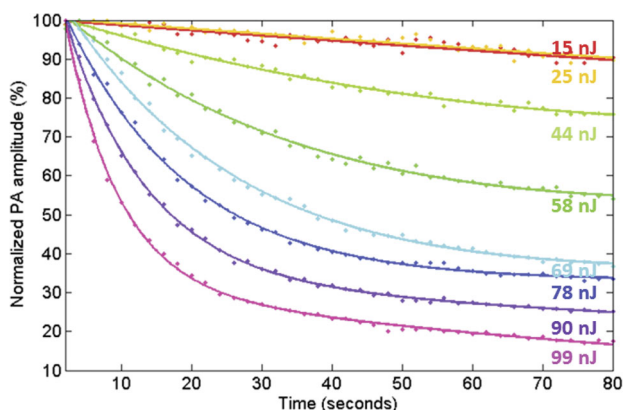


Figure 3 Photothermal bleaching of 400-nm-diameter GNPs under different delivered laser pulse energies. The samples were continuously imaged by PAM at 0.5 Hz C-scan rate.

Figure 4 is a log-log plot of photothermal bleaching rate versus laser pulse energy. Since the photothermal bleaching in PAM originates from instantaneous optical heating, we estimated the temperature rise of a GNP upon a pulse laser excitation and correlated it to the measured photothermal bleaching rate. The light absorption of a spherical GNP obeys Beer's law, which gives

$$\Delta E = \int F(1 - e^{-\mu_a l}) d\sigma = \int_0^{\pi/2} \frac{I}{A} (1 - e^{-\mu_a D \cos \theta}) \pi \frac{D^2}{4} \sin 2\theta d\theta \quad (1)$$

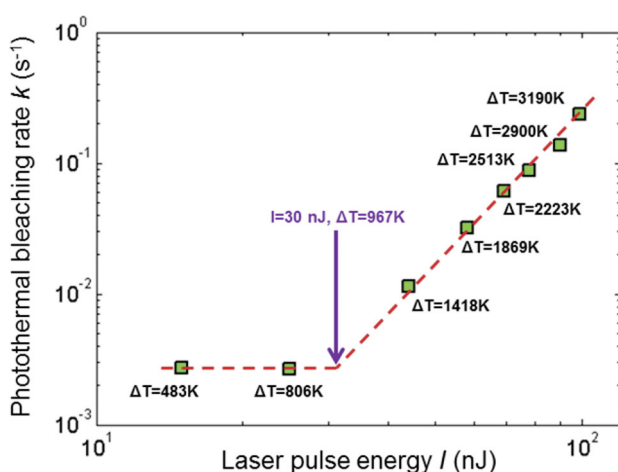


Figure 4 Dependence of photothermal bleaching rate k on the delivered laser pulse energy and temperature rise. I is the laser pulse energy (nJ), and k is the photothermal bleaching rate (s^{-1}). The slope for the data points with pulse energies >30 nJ is 3.6 ± 0.3 (95% confidence bounds). The coefficient of determination, R^2 , is 0.996.

where F is the optical fluence (J/cm^2), σ is the projected cross-section perpendicular to the incident light direction, l is the optical path length, μ_a is the absorption coefficient ($\mu_a^{Au} = 5.6867 \times 10^5 cm^{-1}$), D is the absorber's diameter, I is the laser pulse energy, A is the focal spot area, and θ is the polar angle in the spherical coordinates. Since the thermal confinement time for a 400 nm GNP in water solution is

$$\tau_{th} = \frac{d_c^2}{\alpha_{th}} = \frac{(0.4 \times 10^{-4} cm)^2}{1.3 cm^2/s} = 1.2 ns \quad (2)$$

(d_c is the characteristic dimension of the heated region, and α_{th} is the thermal diffusivity of gold), which is longer than the laser pulse duration (1 ns), the optical heating process was regarded as thermally confined, i.e., thermal conduction was negligible during the pulse laser excitation. Consequently, the temperature rise of a GNP approximates

$$\Delta T = \frac{\Delta E}{C_V \rho V} \quad (3)$$

where C_V is the specific heat ($C_V^{Au} = 0.13 J/g k$), ρ is the mass density ($\rho^{Au} = 19.3 g cm^{-3}$), and V is the volume. By substituting ΔE in Eq. (1) into Eq. (3), the temperature rise ΔT under the excitation of different pulse energies was calculated. The results are shown in Table 1 and labeled next to the corresponding laser pulse energies in Figure 4.

The data in Figure 4 gives two slopes: below $I_c = 30$ nJ, the photothermal bleaching rate k has a weak dependence on the laser pulse energy; while above it, the slope equals 3.6 ± 0.3 , indicating a non-linear relation between photothermal bleaching rate and laser pulse energy $-k \propto I^{3.6}$. The corresponding temperature rise for the critical point $I_c = 30$ nJ was calculated by Eq. (1) and Eq. (3), yielding

$$\Delta T_c = 967 K \quad (4)$$

Assuming the room temperature was $23^\circ C$, the temperature of the GNP after a pulse laser excitation approximated

$$T = T_{room} + \Delta T_c = 990^\circ C \quad (5)$$

Table 1 Calculated temperature rise of a 400 nm diameter GNP upon excitation by different laser pulse energies.

Laser pulse energy (nJ)	Temperature rise (K)
15	483
25	806
44	1418
58	1869
69	2223
78	2513
90	2900
99	3190

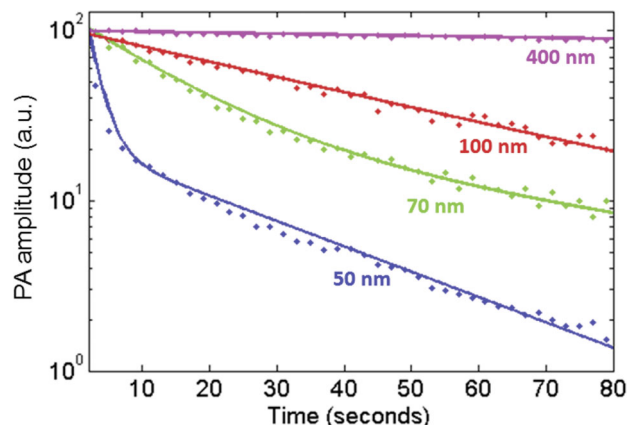


Figure 5 Photothermal bleaching of different diameter GNPs under the same delivered excitation pulse energy (15 nJ). The samples were continuously imaged by PAM at 0.5 Hz C-scan rate.

close to the melting point of gold ($T_{\text{melting}}^{\text{Au}} = 1,064\text{ }^{\circ}\text{C}$). This implies that the phase change of the absorber (from solid to liquid state) may contribute to the two different photothermal bleaching behaviors observed within the linear PA excitation range.

Since photothermal bleaching behaves differently around an absorber's melting point under linear excitation, this dependence suggests an optimal excitation pulse energy for the time-lapse photoacoustic imaging: I_c , the critical value that raises the GNPs to their melting point. Below I_c , raising the excitation pulse energy increases the photoacoustic signal linearly but does not noticeably speed up the photothermal bleaching rate. While above I_c , although increasing the excitation pulse energy can linearly improve

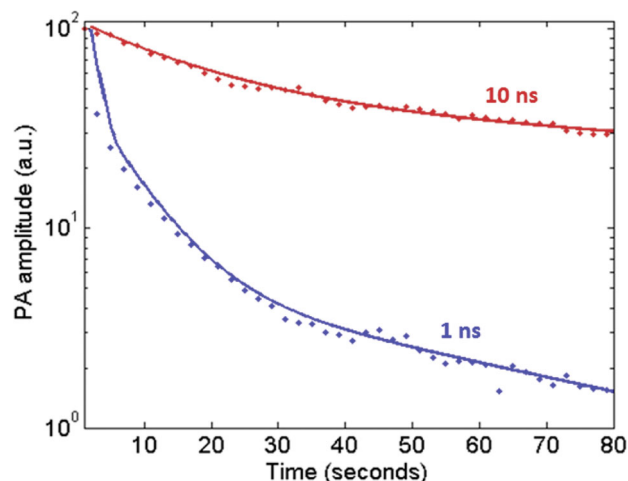


Figure 6 Photothermal bleaching of 100 nm diameter GNPs under two different laser pulse durations. The laser pulse energy delivered was 28 nJ for both pulse durations. The sample was imaged by PAM at 0.5 Hz C-scan rate.

the signal, the photothermal bleaching accelerates nonlinearly, significantly shortening the time window for imaging a dynamic event.

Additionally, the dependence of the photothermal bleaching rate on the absorber's diameter was also investigated. GNPs with diameters of 50 nm, 70 nm, 100 nm, and 400 nm fixed on a glass slide were excited under the same laser pulse energy ($I = 15\text{ nJ}$). The sample was continuously scanned at 0.5 Hz C-scan rate until it became totally photothermally bleached. Figure 5 shows the photoacoustic amplitude versus time for GNPs of different diameters. Because $\mu_a D > 1$ for gold, the energy deposition ΔE is primarily related to D^2 . By contrast, the temperature rise is inversely proportional to D^3 . As a result, smaller particles sustained higher temperature rises and they had faster photothermal bleaching rates than GNPs with larger diameters.

Different laser pulse durations also affect the photothermal bleaching rate. We excited 100-nm-diameter fixed GNPs with two lasers having the same pulse energy (28 nJ) but delivered over different pulse durations (1 ns and 10 ns). As shown in Figure 6, the laser pulses of 1 ns duration bleached the GNPs much faster than the 10 ns ones ($k = 4.40\text{ s}^{-1}$ at 1 ns pulse duration; $k = 0.0775\text{ s}^{-1}$ at 10 ns pulse duration), indicating that pulse duration plays an important role in the photothermal bleaching process. Although the total deposited energy ΔE was the same for both cases, the heat delivered in 10 ns duration diffuses into a larger volume than that delivered in 1 ns duration. Thus the ultimate temperature of GNPs raised by 10 ns laser pulses is lower than that by 1 ns ones. This fact may explain the accelerated photothermal bleaching under illumination by shorter duration laser pulses.

3. Conclusion

In summary, we studied the phenomenon of photothermal bleaching in PAM. The dependence of the photothermal bleaching rate on the excitation laser pulse energy, duration, and absorber's diameter was carefully measured and analyzed. Our results showed that, under linear photoacoustic excitation, two different photothermal bleaching behaviors exist around the absorber's melting point. Based on this finding, an optimal excitation laser pulse energy, which balances the strength of the photoacoustic signal and the bleaching rate, was suggested for time-lapse imaging applications. Additionally, increasing the absorber's diameter or prolonging the laser pulse duration also beneficially reduces the photothermal bleaching rate.

To the best of our knowledge, this is the first time that the phenomenon of photothermal bleaching was

characterized in PAM. This knowledge will be valuable not only for the GNP-based PA imaging, but also for establishing new photothermal-bleaching-assisted techniques such as photoacoustic-recovery after photothermal bleaching or photoacoustic-loss in photothermal bleaching.

4. Materials and methods

4.1 Sample preparation

To eliminate the effect of diffusion during the photothermal bleaching rate measurement, the target GNPs were fixed on top of cover glasses by the following operations [15–17]. The cover glasses were first cleaned in warm detergent (RBS 35, Sigma-Aldrich, USA), flushed with DI water, and dried with nitrogen. Then the cover glasses were put in a plasma oxidizer (Diener Electronics, Germany) for 20 min, followed by another 20 min in a 10% solution of (3-Aminopropyl)-triethoxysilane (Sigma-Aldrich, USA) in anhydrous ethanol. After silanization, the cover glasses were rinsed in anhydrous ethanol and kept at 120 °C for 3 hours. Gold particles with mean diameters of 50 nm, 70 nm, 100 nm (TedPella, USA) and 400 nm (Cytodiagnosics, Canada) were pipetted onto the silanized cover glasses and baked in a 45 °C oven overnight. Before imaging, the samples were washed with DI water on a shaker for 3 hours to remove the unfixed residual gold particles.

4.2 Time-resolved measurement of photothermal bleaching dynamics

Time-resolved photothermal bleaching experiments were performed using a previously described voice-coil scanning PAM [14] with 0.1 NA optical objective. The PAM uses a raster-scanned focused ultrasonic transducer coupled with confocal optical illumination to detect light-absorption-induced ultrasound signals. Two 532-nm-wavelength pulsed lasers (Elforlight, Ltd., UK), with 1 ns and 10 ns pulse durations, respectively, were employed in the photothermal bleaching experiments. The excitation laser pulse energy was adjusted by rotating a variable ND filter (Thorlabs Inc., USA) in front of the laser output, and monitored by a custom-made photodiode. Before the experiment, the correspondence between the laser pulse energy at the sample and the photodiode's measured value was calibrated.

During the photothermal bleaching experiments, the sample was continuously scanned by the PAM at

0.5 Hz C-scan rate until the signals vanished from the image. The image was acquired with 1000 voice coil scanning steps and 20 mechanical stage scanning steps, and rendered as a maximum amplitude projection image. The photoacoustic amplitude of an image was calculated by summing all the signals within the field-of-view ($400 \times 100 \mu\text{m}^2$) after removing the background. The photothermal bleaching rate k was calculated by fitting a double exponential curve $A_{\text{exp}}(-k_1t) + B_{\text{exp}}(-k_2t)$ to the acquired data and averaging over the exponential indices $k = Ak_1 + Bk_2$ [6, 18].

Acknowledgements This work was sponsored by the National Institutes of Health (NIH) under grants R01 EB000712, R01 EB008085, R01 CA134539, U54 CA136398, R01 CA157277, and R01 CA159959. L. V. Wang has a financial interest in Microphotoacoustics, Inc. and Endra, Inc.; however, neither provided support for this work.

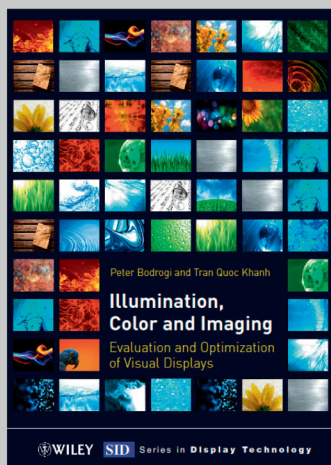
Author biographies Please see Supporting Information online.

References

- [1] R. I. Ghauharali, J. W. Hofstraat, and G. J. Brakenhoff, *J Microsc* **192**, 99–113 (1998).
- [2] R. I. Ghauharali and G. J. Brakenhoff, *J Microsc* **198**, 88–100 (2000).
- [3] E. A. J. Reits and J. J. Neeffjes, *Nat Cell Biol* **3**(6), E145–E147 (2001).
- [4] Y. H. Sniekers and C. C. van Donkelaar, *Biophys J* **89**(2), 1302–1307 (2005).
- [5] J. Lippincott-Schwartz, E. Snapp, and A. Kenworthy, *Nat Rev Mol Cell Bio* **2**(6), 444–456 (2001).
- [6] G. H. Patterson and D. W. Piston, *Biophys J* **78**(4), 2159–2162 (2000).
- [7] L. V. Wang, *Nat Photonics* **3**(9), 503–509 (2009).
- [8] L. H. V. Wang and S. Hu, *Science* **335**(6075), 1458–1462 (2012).
- [9] S. Hu and L. V. Wang, *J Biomed Opt* **15**(1), 011101 (2010).
- [10] Q. Zhang, N. Iwakuma, P. Sharma, B. M. Moudgil, C. Wu, J. McNeill, H. Jiang, and S. R. Grobmyer, *Nanotechnology* **20**(39), 395102 (2009).
- [11] X. M. Yang, E. W. Stein, S. Ashkenazi, and L. H. V. Wang, *Wires Nanomed Nanobi* **1**(4), 360–368 (2009).
- [12] R. Y. Tsien, L. Ernst, and A. Waggoner, *Fluorophores for Confocal Microscopy: Photophysics and Photochemistry*, in: *Handbook of Biological Confocal Microscopy*, J. B. Pawley (Ed.) (Springer, 2006).
- [13] S. Mallidi, T. Larson, J. Tam, P. P. Joshi, A. Karpiouk, K. Sokolov, and S. Emelianov, *Nano Lett* **9**(8), 2825–2831 (2009).
- [14] L. D. Wang, K. Maslov, J. J. Yao, B. Rao, and L. H. V. Wang, *Optics Letters* **36**(2), 139–141 (2011).
- [15] C. George, D. Ricci, and E. Di Zitti, *Superlattice Microsc* **44**(4–5), 608–616 (2008).

- [16] N. Nath and A. Chilkoti, *Anal Chem* **74**(3), 504–509 (2002).
- [17] G. Arslan, M. Özmen, B. Gündüz, X. Zhang, and M. Ersöz, *Turkish Journal of Chemistry* **30**(2), 203–210 (2006).
- [18] S. Gavriluk, S. Polyutov, P. C. Jha, Z. Rinkevicius, H. Agren, and F. Gei'mukhanov, *J Phys Chem A* **111**(47), 11961–11975 (2007).

+++ Suggested Reading +++ Suggested Reading +++ Suggested Reading +++



2012. XXI, 374 pages
Hardcover
224 figures (126 in color.), 58 tables
ISBN 978-3-527-41040-8

BODROGI, PETER / KHANH, TRAN QUOC

Illumination, Color and Imaging

Evaluation and Optimization of Visual Displays

This much needed, comprehensive and modern reference on display technology, illumination sources and color imaging focuses on visual effects and how reproduced images are best matched to human visual features.

As such, it teaches readers how to exploit the knowledge of human color information processing to design usable, ergonomic, and pleasing displays or visual environments. The contents describe design principles and methods to optimize self-luminous visual technologies for the human user, including modern still and motion image displays, and indoor light sources. Design principles and methods

are derived from the knowledge of the human visual system, with a special emphasis on color vision, color cognition, color harmony, color preference and visually evoked emotions. The expert authors include the most important and latest applications of the design principles and methods, forming a comprehensive view of human color information processing from the receptors through the retina via high-level visual perception right up to the level of cognition, preference, harmony, as well as visually evoked emotions.

This book is included in the Wiley SID Series.

Register now for the free
WILEY-VCH Newsletter!
www.wiley-vch.de/home/pas

WILEY-VCH • P.O. Box 10 11 61 • 69451 Weinheim, Germany
Fax: +49 (0) 62 01 - 60 61 84
e-mail: service@wiley-vch.de • <http://www.wiley-vch.de>

WILEY-VCH